Large-Scale Oceanographic Constraints on the Distribution of Melting and Freezing under Ice Shelves

CHRISTOPHER M. LITTLE

Department of Geosciences, Princeton University, Princeton, New Jersey

ANAND GNANADESIKAN AND ROBERT HALLBERG

NOAA/Geophysical Fluid Dynamics Laboratory, Princeton, New Jersey

(Manuscript received 10 October 2007, in final form 11 March 2008)

ABSTRACT

Previous studies suggest that ice shelves experience asymmetric melting and freezing. Topography may constrain oceanic circulation (and thus basal melt–freeze patterns) through its influence on the potential vorticity (PV) field. However, melting and freezing induce a local circulation that may modify locations of heat transport to the ice shelf. This paper investigates the influence of buoyancy fluxes on locations of melting and freezing under different bathymetric conditions. An idealized set of numerical simulations (the "decoupled" simulations) employs spatially and temporally fixed diapycnal fluxes. These experiments, in combination with scaling considerations, indicate that while flow in the interior is governed by large-scale topographic gradients, recirculation plumes dominate near buoyancy fluxes. Thermodynamically decoupled models are then compared to those in which ice–ocean heat and freshwater fluxes are driven by the interior flow (the "coupled" simulations). Near the southern boundary, strong cyclonic flow forced by melt-induced upwelling drives inflow and melting to the east. Recirculation is less evident in the upper water column, as shoaling of meltwater-freshened layers dissipates the dynamic influence of buoyancy forcing, yet freezing remains intensified in the west. In coupled simulations, the flow throughout the cavity is relatively insensitive to bathymetry; stratification, the slope of the ice shelf, and strong, meridionally distributed buoyancy fluxes weaken its influence.

1. Introduction

Fifty percent of the Antarctic coastline is fringed by ice shelves (floating extensions of continental ice sheets), forming a solid boundary over approximately 1.5 million km^2 of the Antarctic continental shelf (Williams 1998). Ice shelves may be sensitive to changes in climatic and oceanic conditions; basal melting may, in turn, influence ice sheet stability and ocean water mass composition (Jacobs et al. 1996; Nicholls 1997; Payne et al. 2004). Assessing the controls on oceanic heat transport and melting in these regions is valuable to glaciologists seeking to determine the role of basal melting in ice sheet mass balance and to oceanographers examining the circulation's sensitivity to change.

Under ice shelves, melting and freezing due to the gradient in the pressure-dependent seawater freezing point drive an overturning circulation that is referred to as the "ice pump" (Lewis and Perkin 1986). The seawater freezing point decreases by about 1°C for each additional kilometer of depth. Maximum rates of melt occur where thermal forcing (difference between the in situ seawater temperature and the pressure-dependent freezing point) is largest—near grounding lines. Meltwater mixes with a much larger volume of ambient water to form a buoyant outflow that can either refreeze as marine ice upon ascent or escape the cavity as a fresh yet dense water mass (Jacobs et al. 1992). In a "closed" ice pump, as envisioned in these experiments, freshwater fluxes associated with melting and freezing are equivalent. Water that refreezes at a higher temperature near the ice shelf front returns to the grounding line and supplies the latent heat necessary to melt ice there.

Recent modeling studies have focused attention on

Corresponding author address: Christopher M. Little, Room 28, Guyot Hall, Department of Geosciences, Princeton University, Princeton, NJ 08544.
E-mail: cmlittle@princeton.edu

DOI: 10.1175/2008JPO3928.1

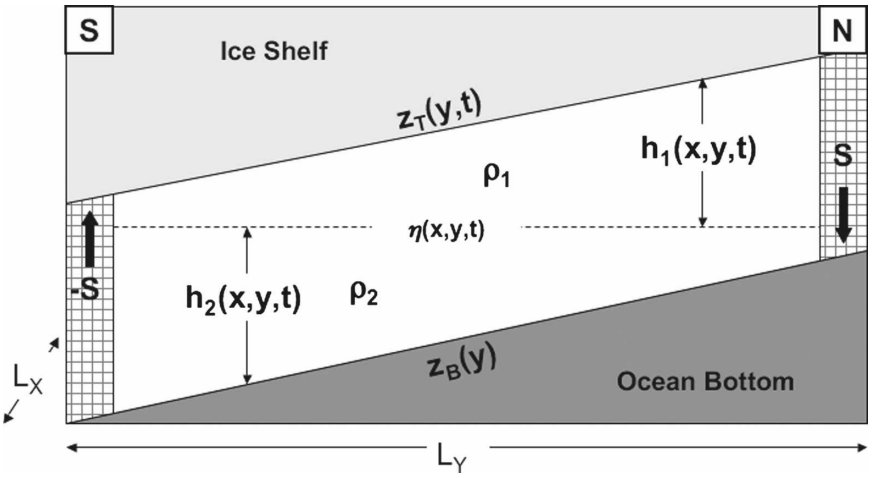

FIG. 1. The two-layer conceptual model used for the decoupled experiments. The model is forced by an equal and opposite diapycnal flux between layers (Hallberg and Gnanadesikan 2001). Near the southern boundary of the domain, $-S$ represents water freshened (and cooled) to the point where its in situ density matches that of the layer above; near the ice shelf front, S represents an implicit loss of freshwater (e.g., brine rejection).

the horizontal distribution of the freezing of marine ice, which appears to be concentrated along western boundaries (Holland 2002; Holland and Feltham 2006). This finding is supported by direct (Oerter et al. 1992) and indirect (Fricker et al. 2001) observations of ice shelves. Although remotely sensed ice-thickness measurements have improved our knowledge of the spatial distribution of mass fluxes, it is difficult to assess the signature of basal melting, particularly near grounding lines (Fricker and Padman 2006). Previous idealized studies of ice shelf cavities (Grosfeld et al. 1997; Holland and Jenkins 2001) suggest that eastern-intensified melting is favored under simplified topographic conditions, implying that "warm," dense water is constrained to flow into these regions.

Although useful as a conceptual framework, the ice pump does not elucidate the dynamics underlying the distribution of melting and freezing. Oceanographic theory suggests that sub–ice shelf conditions—weak stratification, steeply sloped bathymetry, and the presence of a solid surface interface—may enhance topography's role in determining the nature and strength of the horizontal circulation. The focus of these experiments is how thermodynamic forcing interacts with the background potential vorticity field to place dynamic constraints on the circulation.

2. Theory

A conceptual picture of the ice pump can be extended to three dimensions by examining the influence of topography and buoyancy forcing on a linear potential vorticity (PV) balance. The principles of recirculation and intensification in this simplified framework have been discussed in detail in earlier studies (e.g., Stommel 1982); we include this background to aid the interpretation of later experiments. The simplest appropriate model includes two isopycnal (constant density) layers, initially uniform in the zonal (x) direction, forced by opposing mass fluxes in regions of melting and freezing, as illustrated in Fig. 1. The layer thicknesses are given by

$$h_1 = z_T - \eta, \tag{1}$$

$$h_2 = \eta - z_B, \tag{2}$$

where η is the isopycnal interface, and the subscript indicates the isopycnal layer (1 = upper; 2 = lower). The bottom depth, z_B, is constant in time and in the x direction; z_T (the ice–ocean interface) varies in time only because of net convergence of mass in the water column; the ice shelf remains in isostatic equilibrium.

The steady-state, linearized shallow-water equations for each layer consist of a continuity equation that includes a source term (s, positive for fluxes into the lower layer),

$$\nabla \cdot (\mathbf{u}_n h_n) = (-1)^n s, \tag{3}$$

and the horizontal momentum equation for each layer,

$$\mathbf{f} \times \mathbf{u}_n = -\rho_n^{-1} \nabla p_n + \mathbf{F}_n, \tag{4}$$

where f is the Coriolis parameter. Dissipative terms ($\mathbf{F}$) represent ice shelf and bottom drag and/or viscosity.

Substitution of (4) into (3) illuminates the influence of potential vorticity ($q = f/h$) on the flow:

$$h_n \mathbf{u}_n \cdot \nabla(q_n) = -q_n(-1)^n s - h_n \mathbf{k} \cdot (\nabla \times \mathbf{F}_n). \quad (5)$$

Steady flow occurs only along PV contours when the right-hand side of (5) is zero; the location of ageostrophic transport (when **F** is nonzero) is constrained to areas of strong velocity gradients (i.e., boundaries), where PV advection is dissipated. Topography and the Coriolis parameter contribute to the overall PV gradient in each isopycnal layer; in cavities, topography likely dominates. The remainder of this section discusses the influence of topography in a northern region forced by a downward mass flux (representing freezing), a southern region forced by an upward mass flux (melting), and an unforced region in the interior, where $s = 0$ (Fig. 2).

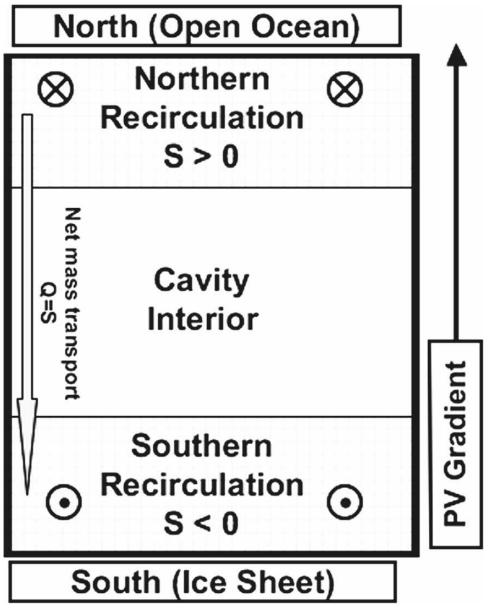

FIG. 2. Schematic illustration of flow regimes in these experiments. The north and south of the domain are characterized by buoyancy fluxes (S), which force meridional transport and a strong recirculation. The unforced region in the interior is assumed to be geostrophic and therefore to carry no meridional transport, except in a lateral boundary layer, with a transport equivalent to the diapycnal flux and a location governed by the PV gradient of the isopycnal layer.

a. Forced regions

Introducing source terms into (3) initiates geostrophic flow in the regions of buoyancy forcing. If meridional topography dominates the PV gradient, (5) simplifies to

$$v_n \frac{\partial h_n}{\partial y} = (-1)^n s, \quad (6)$$

and meridional transport (per unit length) is given by

$$v_n \overline{h_n} = (-1)^n s \overline{h_n} \left(\frac{\partial h_n}{\partial y} \right)_n^{-1}, \quad (7)$$

where $\overline{h_n}$ is the mean layer thickness over the forced region.

At the boundaries of the forced region, $s = 0$; meridional transport (7) must be carried by zonal jets. Integrating zonally from the western (x_w) to the eastern (x_e) limit of the forced region, with a spatially constant source and a constant layer thickness gradient in the source region,

$$M_x = \int_{x_e}^{x_w} v_n \overline{h_n}\, dx = \frac{(-1)^n S \overline{h_n}}{L_y} \left(\frac{\partial h_n}{\partial y} \right)^{-1}, \quad (8)$$

where

$$S = s L_x L_y \quad (9)$$

and L_x and L_y are the zonal and meridional extents of the forced region.

In the presence of a PV gradient, a mass source (s) drives recirculation dominated by strong (M_x) geostrophic jets carrying the integrated transport from and to the forced region. In the absence of other forcing, the circulation in forced regions is cyclonic around a sink of mass (or source of PV) and anticyclonic around a mass source. This combined topographic and planetary β plume is governed by dynamics elucidated in Hallberg and Rhines (1996). Ozgokmen et al. (2001) and Spall (2000) investigate similar regimes when the Coriolis parameter dominates the PV gradient.

b. Interior (unforced) region

In steady state, a cavity-wide density gradient resulting from a coupled source and sink must be balanced by flow through the interior (equivalent to the integrated mass flux S). Ignoring nonlinear terms, interior viscosity, and top and bottom drag, steady meridional transport can only occur where PV advection is dissipated by viscous drag at the lateral boundary. Within this boundary layer (setting $s = 0$, assuming a Laplacian eddy viscosity, and ignoring time dependence and that topography dominates the PV gradient), (5) simplifies to

$$-q_n \mathbf{u} \cdot \nabla h_n = A_H \nabla^2 \zeta_n, \quad (10)$$

where ζ is the horizontal shear across the boundary layer, h is the resting layer thickness, and A_H is the along-isopycnal eddy viscosity.

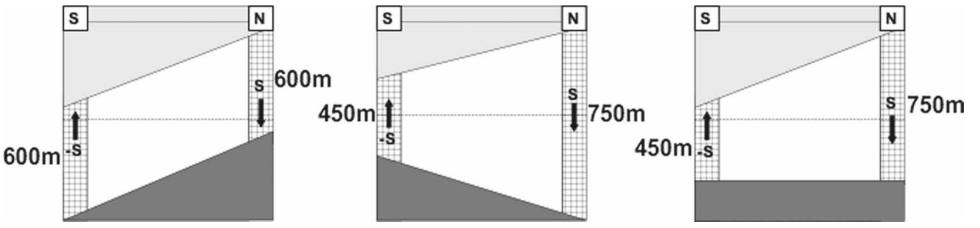

FIG. 3. Meridional cross sections of the (zonally uniform) topographic configurations employed in the decoupled experiments. The idealized topography and parameters used in these experiments are designed to represent a large Antarctic ice shelf cavity. All scenarios have dimensions of 500 km meridionally by 400 km zonally; water column heights at the meridional boundaries are shown. The magnitude of the slope of the ice shelf and ocean floor in the DOWNSLOPE case is half that of the UPSLOPE and FLAT cases. The initial isopycnal interface is shown as a dashed line and divides the cavity volume in half. Hatched regions denote regions of diapycnal flux. A diapycnal mass flux of 0.05 Sv (1 Sv $\equiv 10^6$ m^3 s^{-1})—corresponding to a melt rate of approximately 10^{-3} Sv—is distributed uniformly over the northernmost and southernmost 7.5% of the domain.

If zonal gradients dominate the vorticity balance in the boundary layer ($\partial v/\partial x \gg \partial u/\partial y$), then

$$-q_n v_n \frac{\partial h_n}{\partial y} \sim A_H \nabla^2 \frac{\partial v_n}{\partial x} \sim A_H \frac{\partial^3 v_n}{\partial x^3}. \tag{11}$$

Assigning a scale of $\Delta v \sim \bar{v}$ (the boundary layer velocity) and $\Delta x \sim L_b$,

$$L_b \sim A_H^{1/3} \left(\frac{|f|}{h} \frac{dh}{dy} \right)^{-1/3}. \tag{12}$$

Meridional transport in unforced regions is carried in a boundary current with a width (L_b) that scales inversely with the layer-thickness gradient. If the bathymetry deepens poleward, the boundary current will be found on the east, as Walsh (2002) suggested occurs in Lake Vostok.

Topography's influence in the interior in the numerical experiments may be inferred by the degree and nature of boundary intensification of the interior flow. The role of buoyancy forcing is revealed by the extent of the recirculation (β) plumes, and their influence on the location of meridional transport.

3. Methods

a. Conceptual model

The shape of ice shelves is governed by ice sheet dynamics in the absence of basal traction. Van der Veen (1999) finds that large ice shelves assume a common morphology. Distinct features include a steeply sloped area near the grounding line, a near-vertical ice shelf front, and a steady, relatively steep meridional slope (average slope ranging from 0.5 to 1.5 m km^{-1}). Ice shelf thickness ranges from 1 to 2 km at the grounding line to a few hundred meters at the ice shelf front, with steep side boundaries. Bottom topography under an ice shelf is less uniform and often poorly known. Common features include an upward-sloping (i.e., rising away from the grounding line) continental shelf with a depth near the ice shelf front ranging from 300 to 600 m. Although the continental shelf generally extends beyond the ice shelf front, its geometry is not critical for these experiments due to the lack of an ice front or differentiation of external forcing. A configuration (UPSLOPE) emphasizing these key features of cavity morphology, as well as two variants (FLAT and DOWNSLOPE) designed to illuminate the influence of bathymetry, are used as the domain for the idealized numerical experiments (Fig. 3).

b. Numerical model(s)

These experiments comprise the first set of simulations using the Hallberg Isopycnal Model (HIM) to analyze sub–ice shelf processes. HIM, a National Oceanic and Atmospheric Administration (NOAA)/Geophysical Fluid Dynamics Laboratory (GFDL) ocean model, is a free-surface, hydrostatic, Boussinesq numerical model that solves the primitive equations in isopycnal coordinates. A recent description of the model can be found in Hallberg and Gnanadesikan (2006). Two configurations of HIM are employed (decoupled and coupled). Both have been modified to represent physical processes occurring under ice shelves (Table 1). The coupled simulations utilize a thermodynamically active ice interface (described below), coupled to the isopycnal interior via a bulk mixed layer model (Hallberg 2003).

In all experiments, a temporally and spatially fixed surface pressure field representing an ice shelf floating in isostatic equilibrium is imposed at the ocean surface (Holland and Jenkins 2001). The ice imposes a surface

TABLE 1. Modifications to HIM employed in these experiments.

Physical process	Modification	Reference
Viscous drag	No-slip boundary condition at ice interface	Hallberg and Rhines (1996)
	Quadratic or linear drag law	
	Top boundary layer thickness equal minimum of stratification or rotation limited boundary layer	
	Viscosity of bulk mixed layer set assuming a minimum of ½-layer thickness or top boundary layer thickness; each subsequent isopycnal layer weighted by fraction within top boundary layer	
	Layer velocities solved as system of equations for stress at layer interfaces	
Mixed layer TKE budget	Inclusion of shear-driven turbulence in top boundary layer using a constant conversion factor	Hallberg (2003)
Mixed layer thermodynamic fluxes	Uses a spatially and temporally uniform thermal exchange velocity, γ_T	Holland and Jenkins (1999)
	Meltwater entrained at pressure-dependent freezing point	
Ice shelf conductivity	No conduction into ice shelf—"perfect insulator"	Holland and Jenkins (1999)
Equation of state	Stand-alone linearized equation to calculate pressure-dependent freezing point (in situ)	Foldvik and Kvinge (1974)

stress on the ocean, implemented with a drag law of the form

$$\tau = c_d \mathbf{u}|u|, \tag{13}$$

where c_d is a nondimensional drag coefficient, $\mathbf{u}$ is the velocity in the uppermost layer, and $|u|$ is either a specified background velocity (yielding a linear drag law) or the average flow speed in the upper 10 m of the water column (yielding a quadratic drag law).

In decoupled simulations, a two-layer approximation to the ice pump (similar to Fig. 1) is employed; volume transport of the lower layer is used as an indicator of heat transport to the ice shelf. The only regions of diapycnal flux are equal and opposite, constant, and prescribed. The isopycnal interface does not intersect the ice shelf or bottom boundary in any of the experiments; the minimum initial layer thickness in any of the experiments is 150 m, and no layer disappears in any of the simulations. The reduced gravity at the interface ($9.8\ \mathrm{m\ s^{-2}} \times 10^{-4}\ \mathrm{m\ s^{-2}}$) represents the weak stratification found under ice shelves (e.g., Nicholls et al. 2001). The slope of the shelf and bathymetry is halved in the DOWNSLOPE case to avoid vanishing layers near the southern boundary of the domain. All decoupled simulations were run until a statistically steady-state kinetic energy was achieved (a minimum of 8 yr).

The coupled experiments are initialized with a uniform bulk mixed layer, and 10 isothermal (−1.9°C) isopycnal layers with salinity increasing from 34.4 to 34.8 psu linearly with depth. The circulation is forced solely by heat and freshwater fluxes associated with melting and freezing at the ice interface, described by (14)–(16):

$$Q_M = -\rho_M c_p \gamma_T (T_B - T_M), \tag{14}$$

where Q_M is the diffusive heat flux across the boundary layer between the ice (with a temperature T_B, the depth-dependent seawater freezing point) and the ocean (with an in situ temperature and density in the bulk mixed layer of T_M and ρ_M, respectively), c_p is the heat capacity of seawater, and γ_T is a thermal exchange velocity (Holland and Jenkins 1999). This supplies heat to the ice according to

$$Q_M = \rho_i w L_f, \tag{15}$$

where L_f is the latent heat of fusion of freshwater ice and w is the basal melt (freeze) rate. Combining (14) and (15) provides the freshwater flux to the ice:

$$w = -\frac{\rho_o}{\rho_i}\frac{c_p \gamma_T}{L_f}(T_B - T_M). \tag{16}$$

Though the coupled experiments include heat and momentum fluxes to the ice shelf, neither ice shelf thickness nor its thermodynamic properties evolves with time. No experiment includes an ice shelf front or external forcing. Over the course of these experiments (30 yr, well after melting rates and kinetic energy reach a steady state), the source of heat for melting shifts from the initial heat content of the cavity to that associated with latent heat fluxes to the ice shelf. The ice shelf itself serves as an infinite reservoir of heat. Other key parameters employed in each set of experiments are summarized in Table 2.

4. Results—Decoupled experiments

In the interior of the decoupled simulations (Fig. 4), flow occurs primarily in lateral boundary currents; their

TABLE 2. Key model parameters used in these experiments.

Parameter	Decoupled	Coupled
Domain	400 km (zonal) × 500 km (meridional)	15° lon × 5° lat
Vertical discretization	2 isopycnal layers	Mixed + 10 isopycnal layers
Horizontal resolution	10 km	Isotropic (0.33° longitude)
Drag law	Linear	Quadratic
Seafloor–ice shelf drag coefficient (c_d, unitless)	2.5×10^{-3}	2.5×10^{-3}
Laplacian eddy viscosity coefficient (A_H, m^2 s^{-1})	1.0×10^3	6.0×10^2
Thermal exchange velocity (γ_T, m s^{-1})	None	1.0×10^{-4}

width is slightly underestimated by the scaling of (12), as bottom drag and viscosity not included in the linear analysis dissipate vorticity throughout the cavity. Upper-layer flow across the three scenarios is virtually identical in the interior, indicating that ice shelf geometry ($\partial h_1/\partial y > 0$) forces westward intensification of northward flow. In the lower layer, topography is also sufficient to explain the location of transport in the interior. In the DOWNSLOPE case ($\partial h_2/\partial y > 0$), compression of southward-flowing water columns is balanced by shear adjacent to the western boundary. In the UPSLOPE case ($\partial h_2/\partial y < 0$), southward PV advection is dissipated at the eastern boundary. Although the lower layer of the FLAT case is characterized by a western boundary current, expected in the absence of topography, the strength and width of this current is not fully captured by this scaling, as nonlinear PV advection in regions of intensified flow limits the effectiveness of the simple model described by Fig. 2.

The strong sensitivity to bathymetry observed in the

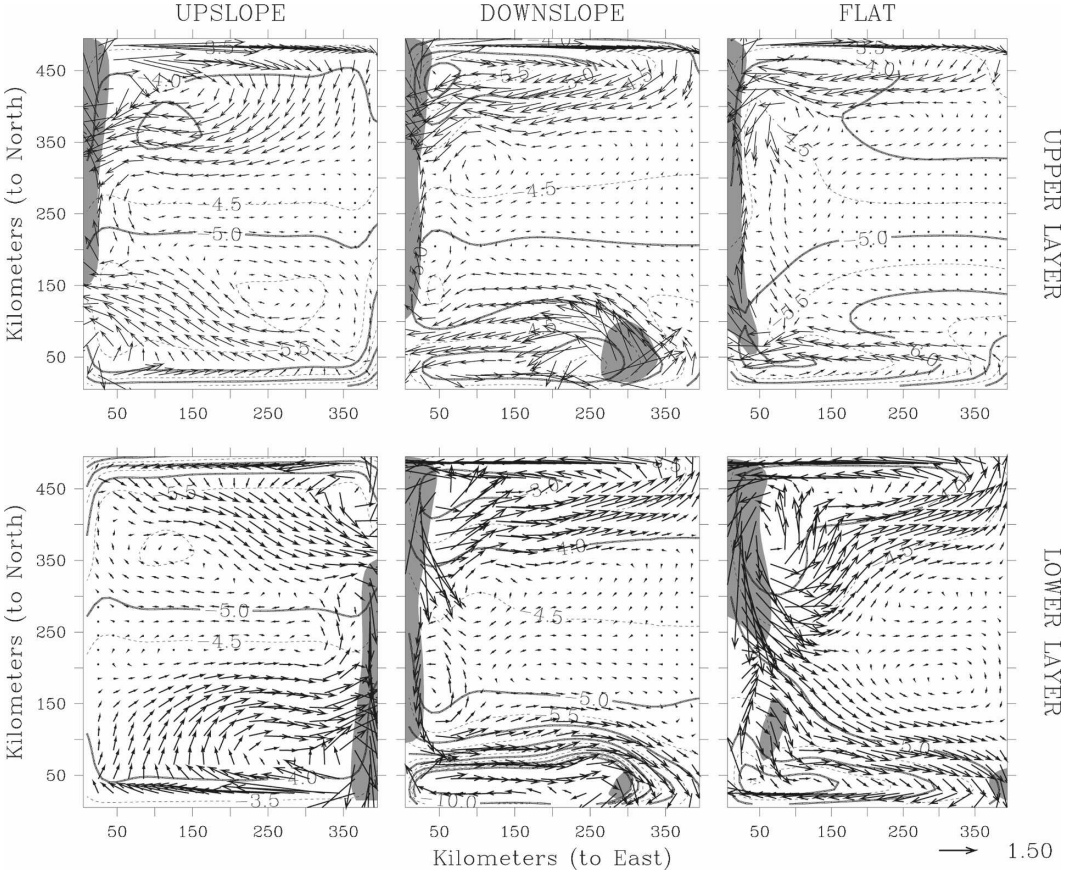

FIG. 4. PV (contours, $\times 10^{-7}$ m^{-1}s^{-1}) and volume transport at grid points (vectors, m^2 s^{-1}) in year 8 of the decoupled experiments: (top) Upper and (bottom) lower layer flow. Shading denotes regions of intensified meridional transport (top) northward and (bottom) southward.

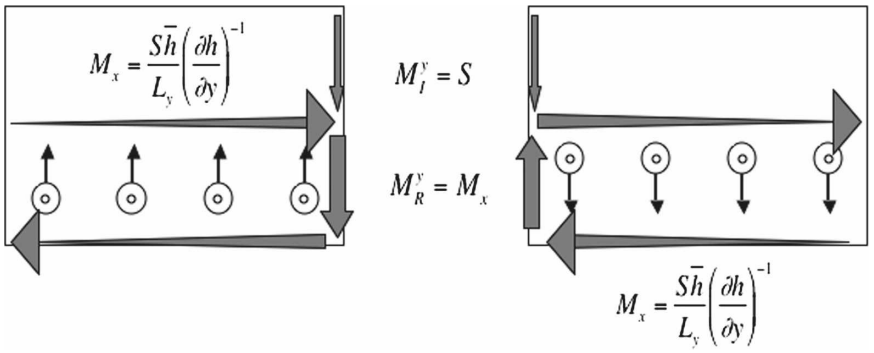

FIG. 5. Schematic illustration of mass fluxes in the southern portion of the lower isopycnal layer in the (left) UPSLOPE and (right) DOWNSLOPE cases. A mass sink in the forced region initiates opposing geostrophic jets in the presence of a PV gradient. To close the mass balance in the forced region, meridional flow at the boundary (where linear geostrophic balance is not valid) must link the two jets and is stronger than the current from the interior. In the DOWNSLOPE case, the recirculation on the western boundary opposes the inflow and diverts southward flow eastward.

interior is not apparent near regions of buoyancy forcing; the orientation of the circulation in forced regions is consistent across all topographic conditions. Near the southern boundary, "melting" ($s > 0$) drives a cyclonic circulation in the lower layer and an anticyclonic flow in the upper layer. In the FLAT and DOWNSLOPE cases, inflow is diverted eastward by recirculation around buoyancy sources. These results contrast with the UPSLOPE case, in which the interior boundary current reinforces the recirculation plume at the eastern boundary. Maxima of southward flow near grounding lines are focused in the southeastern corner in all simulations.

5. Discussion—Decoupled experiments

In large-scale models of buoyancy-driven flow described by (5) and (6), ageostrophic flow closing the circulation is often assumed to be forced by bottom drag acting on the zonal jets. For reasonable drag coefficients, in infinite domains, the zonal (along-PV contour) length scale is far greater than its meridional extent (Ozgokmen and Crisciani 2001). In a cavity, lateral boundaries likely force the closure of the circulation before bottom (or top) drag can dissipate the vorticity anomaly. Assuming that top and bottom drag are minimal, forcing a lateral boundary layer to balance the vorticity flux due to the source

$$\frac{fs}{h} = A_H \frac{\partial^3 v}{\partial x^3} \tag{17}$$

gives a scaling for the transport in the boundary layer:

$$M_R^y \sim v\bar{h}L_b \sim \frac{fSL_b^3}{L_y A_H}. \tag{18}$$

Using (12) and (18),

$$M_R^y \sim \frac{S\bar{h}}{L_y}\left(\frac{\partial h}{\partial y}\right)^{-1}. \tag{19}$$

Unless the layer vanishes over the source region [in which case the linear assumptions used to formulate (19) are invalid], $M_R^y > S$. Equation (19) is equivalent to (8); the transport of the recirculating jets (M_x) is carried in the lateral boundary layer.

Buoyancy-driven recirculation diverts inflow to the southeast, indicating that M_R^y opposes interior flow on the western boundary. The orientation of M_R^y is dependent on the velocity gradient across the lateral boundary layer and the sign of the source term. Because the southern portion of a cavity is characterized by melting (a mass sink for dense layers), positive vorticity fluxes ($s > 0$) in the lower layer advected to the boundary can only be dissipated by a positive velocity gradient across the lateral boundary layer ($\Delta v > 0$)—southward flow on the eastern boundary (as in UPSLOPE) or northward on the western boundary (as in DOWNSLOPE) (Fig. 5). If the recirculation occurs in a lateral boundary layer with equivalent width to the interior boundary current (L_b), the orientation of meridional transport at any boundary is dominated by recirculation rather than by the inflow. With sources distributed across the zonal extent of the cavity, the circulation around regions of buoyancy forcing is unchanged by an opposing PV gradient, is cyclonic at depth in the melting region, and steers southward flow through the interior of the cavity to the eastern boundary (Fig. 5). Though the decoupled

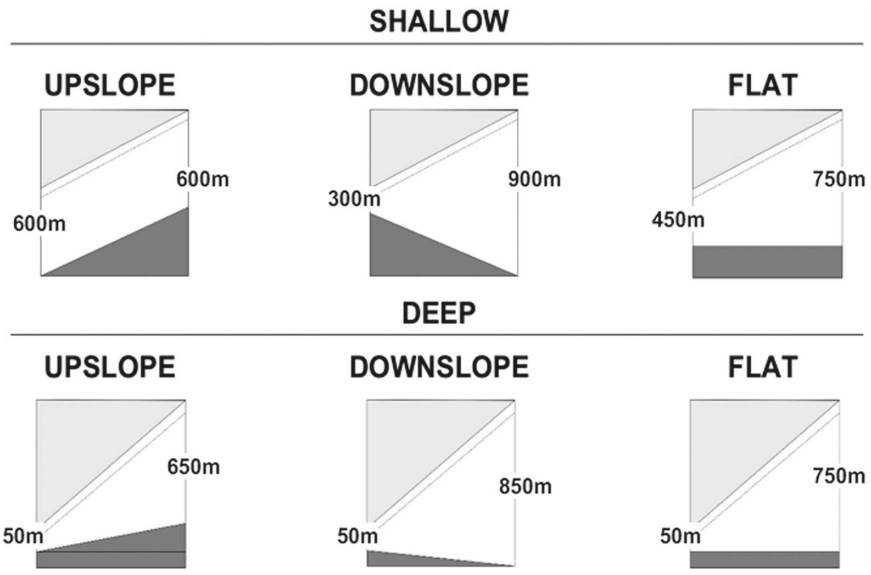

FIG. 6. Same as Fig. 3, but for coupled experiments: (top) SHALLOW and (bottom) DEEP. Note that in these coupled experiments, although the initial stratification is prescribed, isopycnal layers are free to evolve and/or disappear as the cavity circulation reaches a steady state. In each experiment, a bulk mixed layer (Hallberg 2003) coupled to a thermodynamically active ice interface is employed and is shown schematically with a dashed line.

results demonstrate that the relative strength of the two opposing currents is closer than linear scaling predicts (as dissipation and PV advection through the interior weaken the assumptions of this model), northward recirculating flow along the western boundary is always stronger than the inflowing boundary-trapped current, providing the principal explanation for the separation of western boundary currents in the southern portion of the domain.

Although sensitivity studies did not reveal alternative regimes, strong viscosity, bottom drag, or vanishing isopycnal layers ($h \to 0$) increase dissipation and weaken the recirculating plume. In the limiting case in which the anomaly is dissipated within the Munk (or Stommel) layers adjacent to boundaries, the recirculation forced by (7) is eliminated and replaced by a weak zonal flow (Spall 2000).

6. Results—Coupled experiments

Two sets of coupled simulations (illustrated schematically in Fig. 6) were conducted to investigate the validity of the above findings under less idealized conditions. In coupled experiments, melting–freezing locations (and rates) are controlled by the evolution of the flow at depths where heat can access the ice interface. SHALLOW configurations utilize bathymetry identical to the decoupled runs but include a bulk mixed layer, stratification, and thermodynamic fluxes to the ice interface. DEEP configurations include an ice shelf draft that nears the ocean floor at the southern boundary to more closely replicate topographic conditions under ice shelves.

All simulations show relatively little sensitivity to bottom topography (Fig. 7). Distinct regions of melting and freezing are apparent and are concentrated on opposing boundaries—melting (freezing) on the east (west). In all cases, the cavities are characterized by two opposing gyres. Flow in DEEP experiments is more complex, yet in general it is characterized by a stronger, expansive cyclonic gyre. Over time, in all experiments, the zonally averaged density field reveals a circulation characterized by warm, dense inflow at depth and by cold, buoyant outflow in the bulk mixed layer, allowing a comparison with decoupled experiments (Figs. 8a,d). Although the localization of melting is consistent with the simplified dynamics explored earlier, an improved representation of stratification weakens topographic control in the interior. Importantly, in the coupled experiments, meltwater-freshened layers are confined to thin layers adjacent to the ice, revealing a new regime where dissipation minimizes the influence of recirculation.

7. Discussion—Coupled experiments

a. Inflow/melting

These experiments allow freshwater and heat fluxes to migrate. Yet the similarity of the depth-integrated

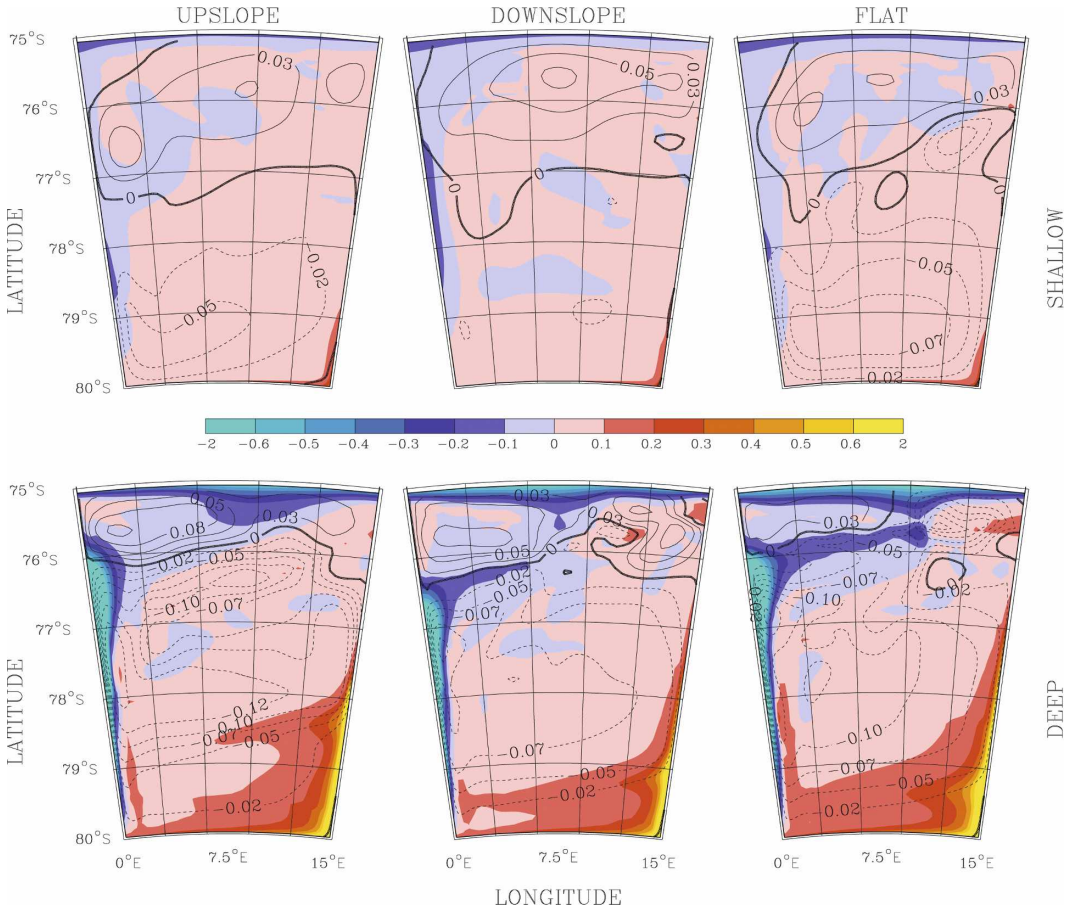

FIG. 7. Barotropic volume transport streamfunction (contours, Sv) and melt rate (shading, m yr^{-1}) in year 30 of the coupled experiments: (top) SHALLOW and (bottom) DEEP. Although the strength of the horizontal circulation varies, melt locations are consistent across the topographic scenarios.

horizontal circulation (which is dominated by cyclonic flow at depth) and locations of intensified melting and freezing (Fig. 7) across differing bathymetric conditions indicates that buoyancy fluxes control the flow at depth, and thus their own spatial distribution. As in the lower layer of the decoupled experiments, southward flow is always diverted to the east by recirculation around regions of melting (Figs. 8c,f); melt rate maxima are found in the southeastern corner of the cavity. During the spinup of each coupled experiment (Fig. 9), the eastward progression of melting occurs within the first year of model integration. Melt-induced upwelling, initially uniform across the southern region of the cavity, establishes a cyclonic gyre at depth that migrates eastward along with the region of melt. Subsequent melting rates are always highest on the eastern boundary and decrease westward.

Well-defined interior boundary currents are not present in SHALLOW simulations, as isopycnal layers below the depth of the ice shelf shield the layers responsible for heat transport to the ice interface. The thickness gradient in intermediate layers (those above the maximum ice shelf draft) is only weakly modified by bathymetry (Fig. 8a). Differing circulation strengths across topographic scenarios indicate that PV remains capable of influencing recirculation at depth; however, participation of deep isopycnal layers in the melt-induced circulation does not influence heat transport to the ice interface. As indicated by Fig. 7, melting rates are unresponsive to changes in volume transport.

The densest isopycnal layers do transport heat to the ice interface in the DEEP configurations, yet bathymetry's influence on these layers (and thus melting) remains muted. Dense layers approach the ice shelf only in the south of the cavity, where the ice shelf draft dominates the layer thickness gradient. Where heat can access the ice interface, the PV gradient remains positive regardless of the imposed bathymetry (Fig. 8d). Although the DOWNSLOPE case shows slightly

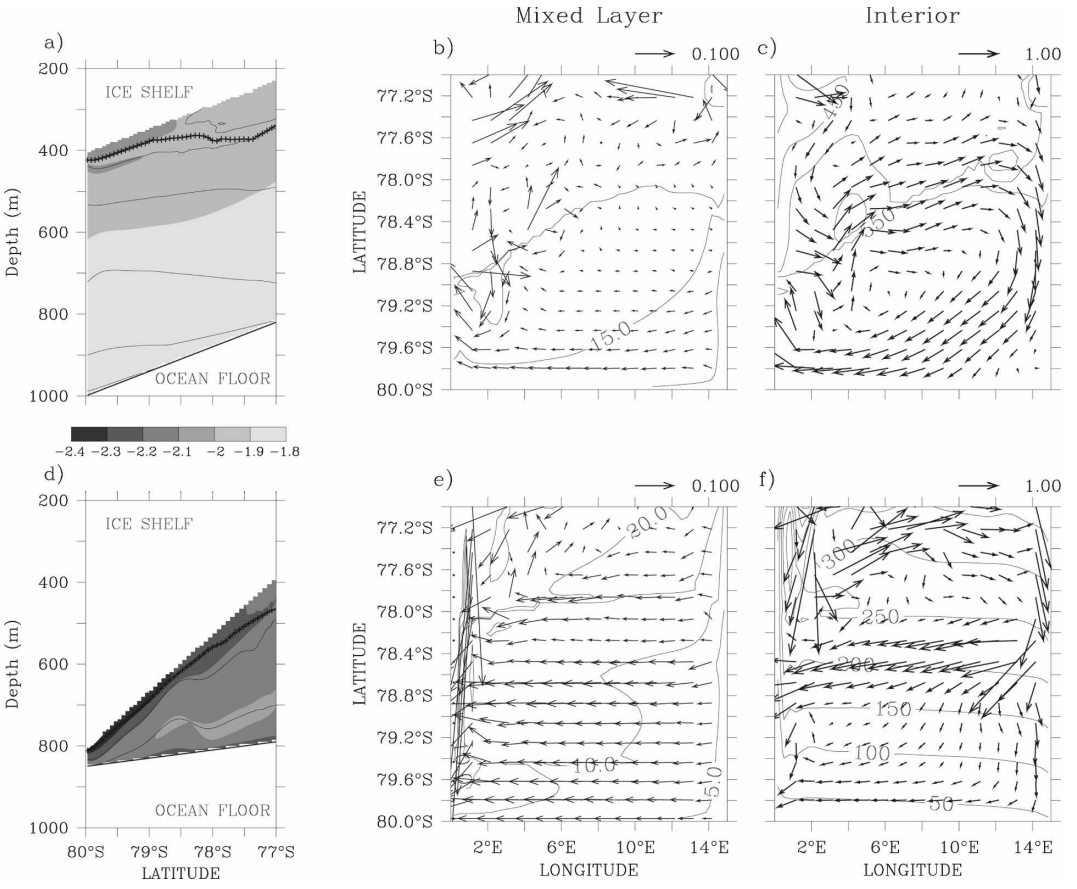

FIG. 8. Comparison of the mixed layer and isopycnal interior in the southernmost 3° of the cavity in year 30 of the UPSLOPE coupled experiments: (top) SHALLOW and (bottom) DEEP. (a), (d) Salinity (contours) and potential temperature (shading) are shown; the bottom of the mixed layer is denoted by the heavy crossed line. The layers responsible for southward heat transport follow the slope of the ice shelf draft in both cases. In the other panels, the volume transport at grid points (vectors, $m^2\ s^{-1}$) in and below the mixed layer is overlaid on the layer thickness (contours, m). (b), (e) Mixed layers are shallow and are characterized by a weak zonal flow and western boundary current, whereas (c), (f) deeper layers are thicker in the southern portions of the domain and are characterized by vigorous recirculation.

weaker meridional flow, it does not impact the distribution of melting.

Perhaps more importantly, there is little evidence of boundary intensification of inflow (and any resultant impact on melting locations), with the increased meridional extent of buoyancy fluxes. Rather than being fixed at the boundaries of the domain (as in the decoupled simulations), buoyancy fluxes gradually decrease from maxima at the meridional boundaries toward the interior of the cavity. Even relatively small melting and freezing rates on the boundary induce a strong zonal flow through the cavity and shift the axis of the induced recirculation northward. Larger and more widespread melt rates in the DEEP experiments force the eastward branch of the recirculation northward by roughly one degree (Figs. 8c,f). The northward excursion of melting eliminates the presence of an unforced region in the coupled experiments; ignoring source terms as in (12) is inappropriate in these cases.

b. Outflow/freezing

Freezing occurs when meltwater-freshened water masses travel northward along the base of the ice shelf. These lighter layers are uniformly thin over the majority of the meridional extent of the cavity and then rapidly thicken in northern regions. The location of intensified freezing (along the western and northern boundaries) is as predicted by the regions of northward flow in the decoupled experiments, yet interior flow is substantially altered. Rather than strong recirculation, layers responsible for meltwater transport (in these simulations, the mixed layer) are characterized by a weak, broad flow along the topographic contours of the ice shelf, freezing as it flows north along the western

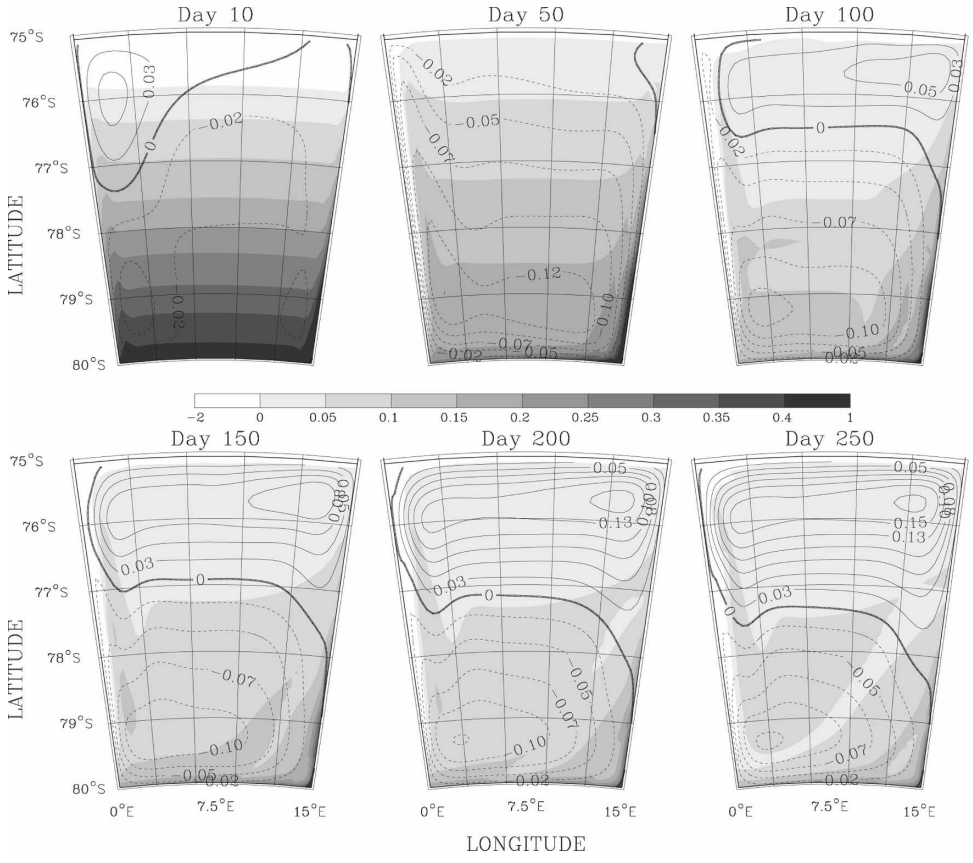

FIG. 9. Snapshots of the barotropic streamfunction (contours, Sv) and melting rates (shading, m yr^{-1}) in the first year of the FLAT, SHALLOW coupled experiment: (top to bottom) Day 10–250. Melt is initially high, zonally uniform, and focused in the south as the initial thermal driving (i.e., in situ temperature of the mixed layer above the in situ freezing point) forces melting. Buoyancy gained by the water column initiates a cyclonic circulation at depth, bringing warmer water into contact with the shelf farther to the east. A cyclonic gyre can be seen dominating the southern half of the cavity after 100 days. As meltwater freezes along the western boundary, the northern gyre strengthens, but inflow on the western boundary continues to be diverted to the interior near the midpoint of the cavity.

boundary (Figs. 8b,e). As the lightest layers shoal in response to meltwater stabilization, dissipation (which increases as the frictional Ekman number, $\nu f^{-1}h^{-2}$) counters the vorticity input responsible for recirculation. The resultant weak zonal flow is indicative of reduced vorticity flux out of the melting region (Spall 2000).

The flow in the mixed layer is driven by the meridional pressure gradient rather than by localized vorticity sources. As predicted by (12), flow is predominantly geostrophic and topographically constrained to flow northward (across PV contours) in a western boundary current. The closed northern boundary in these experiments, which influences both the distribution of freezing as well as the dissipation regime, obscures conclusions about the strength of zonal flow and the nature of recirculation in freezing regions. However, either locally forced recirculation or a topographically driven boundary-trapped outflow will force freezing to the western boundary.

c. Overturning

The overturning circulation in the cavity (Fig. 10) is influenced by both the location and magnitude of buoyancy fluxes. As expected, the principal driver of the strength of overturning circulation is the freezing point gradient; a steeper ice shelf gradient in the DEEP cases drives far stronger overturning in the cavity. Though the imposed topography does influence the melting rates, as well as the strength of the circulation, its influence is moderate and is likely complicated by changes in the volume of the cavity. Interpretation of these results is thus focused on the melting location. Future work may extend these results by examining key parameters (e.g., the ice shelf draft, diffusion, boundary

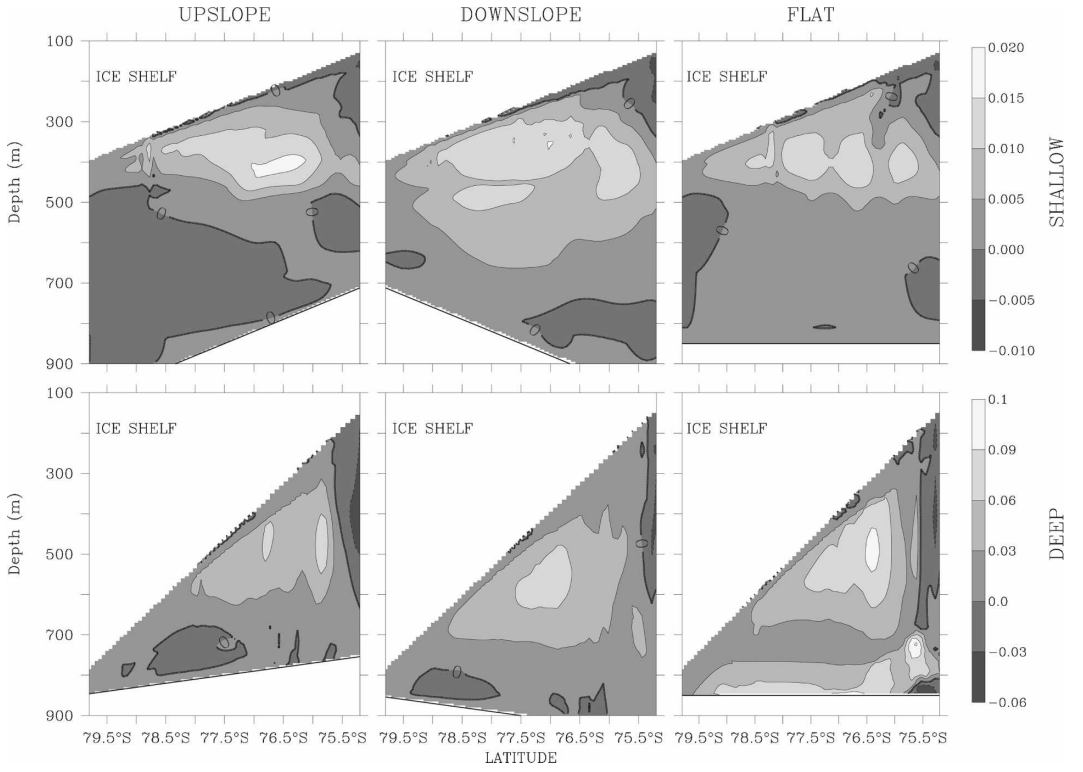

FIG. 10. Overturning volume transport streamfunction (Sv) in year 30 of the coupled experiments: (top) SHALLOW and (bottom) DEEP. The rows use different scales, accounting for stronger overturning in the DEEP runs.

layer turbulence) controlling the strength of the overturning circulation in simplified or complex models.

d. Comparison with previous results

Vorticity dynamics have not generally been employed in the interpretation of ice shelf cavity circulation. One exception is Grosfeld et al.'s (1997) analysis, in which the PV barrier imposed by the ice shelf front limits inflow to regions of constant water column heights. Our results show that PV can also provide a cohesive dynamic framework to understand the distribution of ice–ocean fluxes found in other idealized studies. Both along-PV contour flow *and* PV dissipation regimes (as governed by the layer thickness and buoyancy flux) govern favored locations of ice–ocean heat flux.

Recent model studies (Holland and Feltham 2006; Payne et al. 2007) have emphasized the importance of meltwater-freshened near-ice plume dynamics in governing the rate and location of buoyancy fluxes. Though the dynamics of turbulent mixing near the ice interface are likely important, particularly under conditions of ample heat and strong outflow, our simulations indicate that inflow at depth is a strong determinant of melting locations. Without a deep source of heat, boundary layer turbulence is not sufficient to sustain melting. Although a number of studies have shown eastern intensification of melting (Grosfeld et al. 1997; Holland and Jenkins 2001; Holland 2002; Holland and Feltham 2006), our analysis offers a clearer mechanism to connect melting and freezing regimes. In agreement with Holland and Jenkins (2001) and Holland and Feltham (2006), we attribute western-intensified freezing to ice shelf topography; the absence of recirculation is driven by the thermodynamic response of the upper-water column in melting regions. Geostrophic flow, coupled to dissipation of the vorticity source, drives western intensification.

The strong similarity of sub-ice-shelf circulation and ice–ocean fluxes across idealized models indicates a common dynamic constraint. Because the oceanic PV field underneath ice shelves is likely dominated by ice shelf geometry, and ice shelves share similar forcing (i.e., melting at depth), these model results suggest that asymmetric heat delivery may persist across more realistic topography.

8. Summary and conclusions

Ice shelf cavities are highly inaccessible regions of the world's oceans, yet they may have a role in regulating

climate and sea level. The effort required to obtain in situ measurements, particularly in the vicinity of ice sheet grounding lines, requires guidance from model studies of varying complexity. These experiments attempt to use simple models to understand the distribution of melting and freezing, with a goal of providing insight to further observational and modeling efforts. The specified oceanic regime is most relevant to the circulation under large ice shelves, where heat is confined to the densest water masses on the continental shelf.

In these experiments, zonal asymmetry in melting and freezing patterns is controlled by different dynamic constraints, neither of which is strongly influenced by bathymetry. At depth, buoyancy fluxes force bathymetry-independent horizontal recirculation resulting from vertical motion in the presence of PV gradients. Linear, steady-state scaling considerations suggest that the strength of the induced recirculation dominates topographically constrained interior mass transport. This hypothesis is confirmed by primitive equation numerical models using spatially fixed diapycnal fluxes. Southward heat flux is diverted by a cyclonic circulation at depth, forcing melting to the east regardless of the flow in the interior. With an improved representation of stratification and freely evolving thermodynamic fluxes, the primary findings of the two-layer model hold—the dynamics of dense, warm layers and light, cold layers are well separated and drive melting and freezing, respectively. Yet the flow in meltwater-freshened layers is influenced by shoaling, which dissipates the buoyancy forcing, resulting in relatively weak along-slope flow. Outflow (and freezing in coupled experiments) is thus confined to the western boundary and is principally controlled by the ice shelf draft. Although dissipation sufficient to weaken recirculation is not evident in deeper layers, it may influence southward heat transport should inflow be restricted to thin, bottom-trapped layers.

Underneath ice shelves, the ocean is characterized by diverse forcing and complex topography. Spatially and temporally variable dynamics (notably tides) may decouple heat sources and the response of flow at depth. Unique topographic conditions under ice shelves may modify the scale and strength at which these phenomena are manifested. The ice shelf may also respond dynamically to melting, modifying the flow and thus the melting/freezing pattern. These processes have not been captured; these idealized experiments simplify this small-scale, often poorly characterized variability to focus on steady, large-scale dynamic controls. Yet the demonstrated insensitivity to bathymetry, dissipative parameterizations, and forcing strength suggests that asymmetry in the circulation and melt rate may exist to varying degrees under ice shelves. It is our hope that these hypotheses can be validated with fast-improving observations of melting and freezing and, if supported, can be used to guide future observational efforts, as well as be used as a base for comparison with more comprehensive numerical experiments incorporating more complex topography and mixing conditions.

Acknowledgments. We thank GFDL for the use of its computing resources and advice from its community, particularly the helpful reviews of Sonya Legg and Mike Winton. CML would like to thank Michael Oppenheimer for guidance, David Holland and Stan Jacobs for their thoughts and encouragement, and Michael Dinniman and Harmut Hellmer for comments on this manuscript. CML receives research funding from GFDL (through the Cooperative Institute for Climate Science), the Science, Technology, and Environmental Policy program in the Woodrow Wilson School of Public and International Affairs at Princeton University, and the U.S. Environmental Protection Agency Science to Achieve Results (EPA STAR) graduate fellowship program. EPA has not officially endorsed this publication and the views expressed herein may not reflect the views of the EPA.

REFERENCES

Foldvik, A., and T. Kvinge, 1974: Conditional instability of sea water at the freezing point. *Deep-Sea Res.,* **21,** 169–174.

Fricker, H. A., and L. Padman, 2006: Ice shelf grounding zone structure from ICESat laser altimetry. *Geophys. Res. Lett.,* **33,** L15502, doi:10.1029/2006GL026907.

——, S. Popov, I. Allison, and N. Young, 2001: Distribution of marine ice beneath the Amery Ice Shelf. *Geophys. Res. Lett.,* **28,** 2241–2244.

Grosfeld, K., R. Gerdes, and J. Determann, 1997: Thermohaline circulation and interaction between ice shelf cavities and the adjacent open ocean. *J. Geophys. Res.,* **102,** 15 595–15 610.

Hallberg, R., 2003: The suitability of large-scale ocean models for adapting parameterizations of boundary mixing and a description of a refined bulk mixed layer model. *Near Boundary Processes and Their Parameterization: Proc. 2003 'Aha Huliko'a Hawaiian Winter Workshop,* Honolulu, HI, University of Hawaii at Manoa, 187–203.

——, and P. Rhines, 1996: Buoyancy-driven circulation in an ocean basin with isopycnals intersecting the sloping boundary. *J. Phys. Oceanogr.,* **26,** 913–940.

——, and A. Gnanadesikan, 2001: An exploration of the role of transient eddies in determining the transport of a zonally reentrant current. *J. Phys. Oceanogr.,* **31,** 3312–3330.

——, and —— 2006: The role of eddies in determining the structure and response of the wind-driven Southern Hemisphere overturning: Results from the Modeling Eddies in the Southern Ocean (MESO) project. *J. Phys. Oceanogr.,* **36,** 2232–2252.

Holland, D. M., 2002: Computing marine-ice thickness at an ice-shelf base. *J. Glaciol.,* **48,** 9–19.

——, and A. Jenkins, 1999: Modeling thermodynamic ice–ocean interactions at the base of an ice shelf. *J. Phys. Oceanogr.,* **29,** 1787–1800.

——, and ——, 2001: Adaptation of an isopycnic coordinate ocean model for the study of circulation beneath ice shelves. *Mon. Wea. Rev.,* **129,** 1905–1927.

Holland, P. R., and D. L. Feltham, 2006: The effects of rotation and ice shelf topography on frazil-laden ice shelf water plumes. *J. Phys. Oceanogr.,* **36,** 2312–2327.

Jacobs, S. S., H. Hellmer, C. S. M. Doake, A. Jenkins, and R. Frolich, 1992: Melting of ice shelves and the mass balance of Antarctica. *J. Glaciol.,* **38,** 375–387.

——, H. H. Hellmer, and A. Jenkins, 1996: Antarctic ice sheet melting in the Southeast Pacific. *Geophys. Res. Lett.,* **23,** 957–960.

Lewis, E. L., and R. G. Perkin, 1986: Ice pumps and their rates. *J. Geophys. Res.,* **91,** 11 756–11 762.

Nicholls, K. W., 1997: Predicted reduction in basal melt rates of an Antarctic ice shelf in a warmer climate. *Nature,* **388,** 460–462.

——, S. Østerhus, K. Makinson, and M. R. Johnson, 2001: Oceanographic conditions south of Berkner Island, beneath Filchner-Ronne Ice Shelf, Antarctica. *J. Geophys. Res.,* **106,** 11 481–11 492.

Oerter, H., J. Kipfstuhl, J. Determann, H. Miller, D. Wagenbach, A. Minikin, and W. Graf, 1992: Evidence for basal marine ice in the Filchner-Ronne Ice Shelf. *Nature,* **358,** 399–401.

Ozgokmen, T., and F. Crisciani, 2001: On the dynamics of beta plumes. *J. Phys. Oceanogr.,* **31,** 3569–3580.

——, E. Chassignet, and C. Rooth, 2001: On the connection between the Mediterranean outflow and the Azores Current. *J. Phys. Oceanogr.,* **31,** 461–480.

Payne, A. J., A. Vieli, A. Shepherd, D. J. Wingham, and E. Rignot, 2004: Recent dramatic thinning of largest West Antarctic ice stream triggered by oceans. *Geophys. Res. Lett.,* **31,** L23401, doi:10.1029/2004GL021284.

——, P. R. Holland, A. P. Shepherd, I. C. Rutt, A. Jenkins, and I. Joughin, 2007: Numerical modeling of ocean-ice interactions under Pine Island Bay's ice shelf. *J. Geophys. Res.,* **112,** C10019, doi:10.1029/2006JC003733.

Spall, M., 2000: Buoyancy-forced circulations around islands and ridges. *J. Mar. Res.,* **58,** 957–982.

Stommel, H., 1982: Is the South Pacific Helium-3 plume dynamically active? *Earth Plan. Sci. Lett.,* **61,** 63–67.

Van der Veen, C. J., 1999: *Fundamentals of Glacier Dynamics*. Balkema, 462 pp.

Walsh, D., 2002: A note on eastern-boundary intensification of flow in Lake Vostok. *Ocean Modell.,* **4,** 207–218.

Williams, M., 1998: Physical controls on the ocean circulation beneath ice shelves revealed by numerical models. *Oceans, Ice and Atmosphere: Interactions at the Antarctic Continental Margin,* S. Jacobs and R. Weiss, Eds., Amer. Geophys. Union, 285–299.